This article has been accepted for publication in a future issue of this journal, but has not been fully edited. Content may change prior to final publication. Citation information: DOI 10.1109/TMECH.2017.2717874, IEEE/ASME Transactions on Mechatronics

Design of a Parallel Actuated Exoskeleton for Adaptive and Safe Robotic Shoulder Rehabilitation

Hsiang-Chien Hsieh, Dian-Fu Chen, Li Chien, and Chao-Chieh Lan, *Senior Member*, *IEEE*

***Abstract*—Powered exoskeletons can facilitate after-stroke rehabilitation of patients with shoulder disabilities. Designs using serial mechanisms usually result in complicated and bulky exoskeletons. This paper presents a new parallel actuated shoulder exoskeleton that consists of two spherical mechanisms, two slider crank mechanisms, and a gravity balancing mechanism. The actuators are grounded and placed side-by-side. Thus better inertia properties can be achieved while lightweight and compactness are maintained. An adaptive mechanism with only passive joints is introduced to compensate for the exoskeleton-limb misalignment and size variation among different subjects. Linear series elastic actuators (SEAs) are proposed to obtain accurate force and impedance control at the exoskeleton-limb interface. The total number of force sensors and actuators is minimized using the adaptive mechanism and SEAs. An exoskeleton prototype is shown to provide bidirectional actuation between the exoskeleton and upper limb, which is required for various rehabilitation processes. We expect this design can provide a means of shoulder rehabilitation.**

***Index Terms*—Shoulder rehabilitation, upper limb exoskeleton, parallel spherical mechanism, series elastic actuator, axis misalignment, adaptive mechanism, impedance control.**

I. Introduction

REHABILITATION of after-stroke patients with shoulder disabilities requires repeated and progressive training exercise. To reduce the cost of therapist labor, it is necessary to use robots to facilitate rehabilitation training of various intensity levels. Powered exoskeletons of multiple degrees-of-freedom (DOFs) have been developed to assist the motion of human upper limbs [1-4]. Compared with joints of the lower limbs, human upper limb joints are smaller in size. They are more dexterous because they provide motion in both the coronal and sagittal planes. Various designs have been proposed to augment the motion of shoulder [5], elbow [6], wrist [7], or the whole upper limb [1-4, 8-12].

Although the majority of existing exoskeletons uses electric motors with gearboxes of high reduction ratios [1, 3-4], their actuator weights are still considerable. A multi-DOF exoskeleton usually employs a serial mechanism [1-4, 8-11] whose rotation axes match with the joint axes of an upper limb. This type of design offers sufficient dexterity to resemble the motion of an upper limb. If gravity-balancing mechanisms [1, 2, 9, 11] were not used, the weight of the human arm and hanging motors need to be supported by the links and motors close to the base link. Hence these proximal links and motors must be large enough to ensure good dynamic property of the whole exoskeleton. Some exoskeletons explored parallel mechanisms [7-9] or flexible mechanisms [5, 12] to reduce the inertia problem but the size and complexity remained an issue. It is still a challenging task for existing exoskeletons to be lightweight and compact.

Different from end-effector type rehabilitation robots (e.g., [13]), exoskeletons are designed to align their rotation axes with those of human limbs in order to provide motion assistance. This offers two advantages: direct limb force/motion control and singularity avoidance. However, these advantages rely on precise alignment of exoskeleton axes with those of human limbs. When misaligned, unwanted exoskeleton forces would impose on human limbs, which cause discomfort and even injury. Because human skeleton, tendons, and muscles are complex and deformable, their geometry and kinematics can never be perfectly modeled. In addition, different subjects have different bone/muscle sizes and thus joint kinematics. Improper mounting of an exoskeleton on a human limb and undesirable human motion during exoskeleton-limb interaction would also occur. Hence misalignment of an exoskeleton is unavoidable.

From kinematics point of view, an exoskeleton and human limb form a highly over-constrained system. Thus any small misalignment would generate undesirable forces between an exoskeleton and human limb. Adding compliance at the exoskeleton-limb interface could reduce the harming force but the exoskeleton rigidity would be compromised. Changing the geometry (by adding adjustable components) of exoskeletons [1, 14] to adapt to subjects of different sizes can minimize the misalignment due to subject variation. However, this approach cannot account for the misalignment due to un-modeled limb kinematics. Adding more active joints [3, 4] can match closer with limb kinematics but would complicate the exoskeleton. A more promising approach is to introduce mobility between exoskeleton and human limb. This can be achieved using multiple passive joints [15-16]. The relative displacements of the passive joints are used to adapt to the misalignments.

For an exoskeleton to interact safely with a human limb, it is important to measure and control the interaction force. Previous research (see [17] for a comprehensive review) used signals from pressure [18] or force sensors [1-3] as the feedback to control the motion of exoskeletons. To further reduce the interface impedance, series elastic actuators (SEAs) were used. By controlling the deformation of a serially connected elastic element, an SEA can provide accurate force control, back-drivability, and adjustable impedance without using additional force sensors [19-20]. SEAs have been used in serial shoulder exoskeletons [2, 4, 21] but have not yet been realized in parallel shoulder exoskeletons.

This work was supported by the Ministry of Science and Technology, Taiwan (with Project No. MOST 105-2221-E-006-095). H.-C. Hsieh, L. Chien, D.-F. Chen, and C.-C. Lan are with the Department of Mechanical Engineering, National Cheng Kung University, No. 1, University Rd., Tainan, Taiwan. (corresponding author e-mail: cclan@mail.ncku.edu.tw).

This article has been accepted for publication in a future issue of this journal, but has not been fully edited. Content may change prior to final publication. Citation information: DOI 10.1109/TMECH.2017.2717874, IEEE/ASME Transactions on Mechatronics

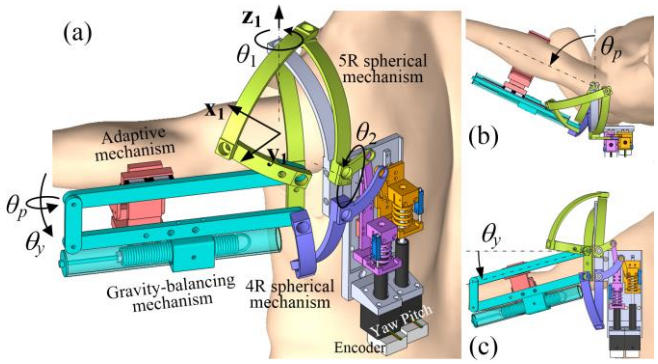

Fig. 1 (a) CAD model of the shoulder exoskeleton worn on a human's left arm (b) Pitch motion (c) Yaw motion

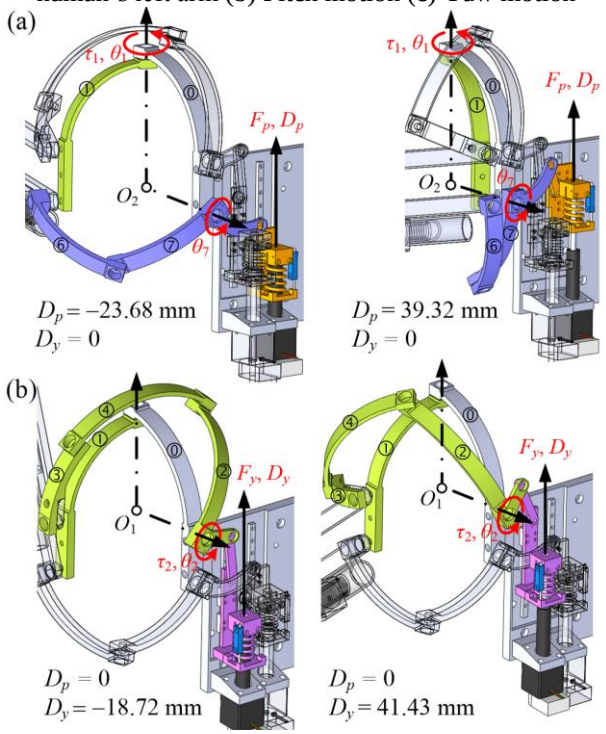

Fig. 2 (a) Pitch actuation (b) Yaw actuation

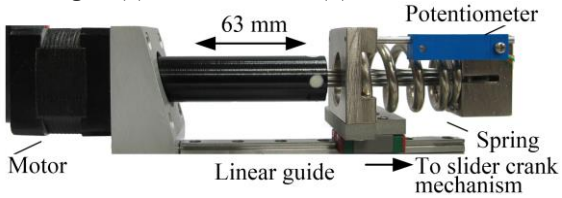

Fig. 3 Linear SEA

Aimed at providing an effective and friendly after-stroke shoulder rehabilitation, this paper proposes a parallel actuated exoskeleton with two active and four passive DOFs. This exoskeleton includes two linear SEAs for the interaction force control. Two spherical mechanisms and a gravity-balancing mechanism are used to minimize the load on the motors and increase the device compactness. An adaptive mechanism is installed between the upper arm and exoskeleton. It offers four passive DOFs to adapt to any misalignment between the upper arm and exoskeleton. In what follows, we first describe the details of the exoskeleton in Sec. II. The kinematics and statics are presented in Sec III. Sec. IV presents the design of the adaptive mechanism. Finally, dynamic modeling and control experiments of a prototype are presented in Sec. V.

Table 1 Comparison of exoskeleton specifications

	[1]	[2]	[9]	Ours
Pitch range (°)	182	120	99	95
Yaw range (°)	94	120	73	110
Pitch torque (Nm)	33 (max.)	36 (max.)	77 (max.)	44 (ave.)
Yaw torque (Nm)	38 (max.)	36 (max.)	50 (max.)	24 (ave.)
Active DOFs	4	4	4	2
Passive DOFs	0	4	0	4
Actuator type	Electric	Hydraulic	Pneumatic	Electric
Total weight (kg)	18.8	8	4.4	4

II. Description of the Shoulder Exoskeleton

2.1 Spherical and slider crank mechanisms

Fig. 1(a) shows the CAD model of the proposed shoulder exoskeleton. There are two identical linear motors attached to the ground. The pitch motor provides the pitch motion in the horizontal plane as shown in Fig. 1(b), whereas the yaw motor provides the yaw motion in the vertical plane as shown in Fig. 1(c). These two DOFs offer the dexterity for the shoulder to have flexion/extension and abduction/adduction motion. Table 1 lists the comparison of ours with other entire-arm exoskeletons. For our exoskeleton, the achieved pitch range is $\theta_p = -20°$ to 75° and yaw range is $\theta_y = -40°$ to 70°. The pitch motion range of ours is smaller than that in [1] but comparable to those in [2, 9]. The yaw motion range is larger than those in [1, 9]. The motion range can cover the majority of shoulder activities in daily lives (Pitch range = 180° and yaw range = 90°) [1].

Fig. 2 shows how the pitch and yaw motions are generated. Link numbers are circled. In Fig. 2(a), the pitch motor displacement D_p is transmitted to provide the input pitch angle θ_1 along the $\mathbf{z}_1$ axis through the pitch slider crank mechanism (pitch mechanism) and the 4R spherical mechanism, which includes Links 0, 1, 6, and 7. The pitch motor force and input pitch torque are F_p and τ_1, respectively. In Fig. 2(b), the yaw motor displacement D_y is transmitted to provide the input yaw angle θ_2 along the $\mathbf{x}_1$ axis through the yaw slider crank mechanism (yaw mechanism). The yaw motor force and input yaw torque are F_y and τ_2, respectively. Through the 5R spherical mechanism formed by Links 0-4, input rotations θ_1 and θ_2 are transformed to output rotations θ_p and θ_y of the gravity-balancing mechanism. As shown in Fig. 1(a), the exoskeleton is connected to a human's upper arm via an adaptive mechanism. The two axes of input rotation intersect perpendicularly at the center (O_1) of the 5R spherical mechanism. The center of the 4R spherical mechanism is denoted as O_2 and is directly underneath O_1. The exoskeleton center O_1 is to align with the center of a human's shoulder joint.

2.2 Linear SEAs

To achieve safe interaction, two identical linear SEAs are used to respectively provide the pitch and yaw motion. Fig. 3 shows a prototype of the linear SEA. The linear stepper motor (Haydon, size 14) has a maximum force of 220 N and stroke of 63 mm with an encoder behind the motor to record the

This article has been accepted for publication in a future issue of this journal, but has not been fully edited. Content may change prior to final publication. Citation information: DOI 10.1109/TMECH.2017.2717874, IEEE/ASME Transactions on Mechatronics

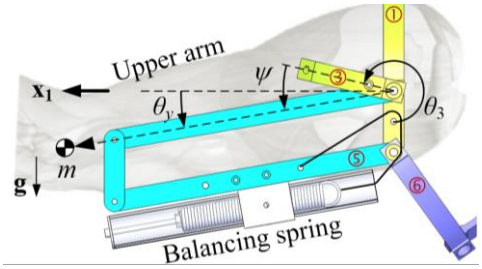

Fig. 4 Gravity-balancing mechanism

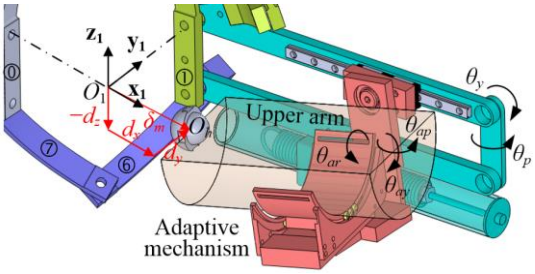

Fig. 5 Shoulder misalignments and adaptive mechanism

output displacement. The motor is serially connected to a spring with measured stiffness of 33 N/mm. The other end of the spring is connected to a slider crank mechanism. The deformation of the spring is measured using a potentiometer (BOURNS 3048L-5-502) to obtain the spring force, which can be used to estimate the interaction force between the exoskeleton and upper arm. Thus accurate force or impedance control can be realized without using external force/torque sensors. This makes the exoskeleton more compact.

Because the motors are mechanically grounded, alternative motors of larger sizes could be used for the SEA without causing inertia or interference problems. We have evaluated a bigger motor (Haydon, size 23) that has a maximum force of 890 N. If this bigger motor were used, the average pitch and yaw torques could reach up to 44 Nm and 24 Nm, respectively, which are comparable to others listed in Table 1.

2.3 Gravity balancing and adaptive mechanisms

The gravity-balancing mechanism shown in Fig. 4 is a parallelogram linkage whose proximal short link is part of Link 1. The top long link is rigidly connected to Link 3. A coil spring with measured stiffness of 1.88 N/mm is attached to the bottom of the linkage with pulleys and cables. The spring is preloaded in order to emulate the condition of a zero-free-length spring. When ideally designed, it can provide full support for the weight of the upper limb so that the upper limb can move freely in the yaw direction. This can further reduce the yaw motor size and energy loss. The change of elbow angle can be shown to have only minor effect on the balancing property [22]. If required, the stiffness of the balancing spring can be easily adjusted to fit different arm weights. Detailed design of the gravity balancing mechanism can be found in [22].

The adaptive mechanism shown in Fig. 5 is connected to the top long link of the gravity balancing mechanism. On top of the adaptive mechanism is a semi-cylinder with a spherical joint used to model a human shoulder and upper arm. When the shoulder joint center O_h and exoskeleton center O_1 are not aligned, the adaptive mechanism provides four passive joints

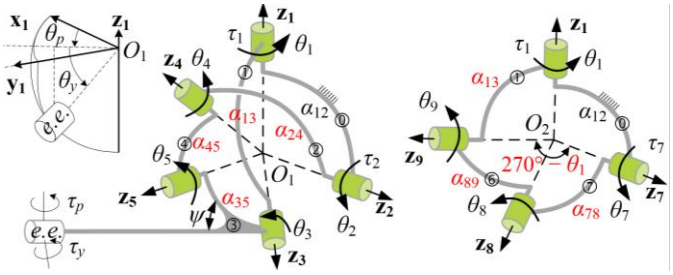

Fig. 6 Diagrams of the 5R and 4R spherical mechanisms

to adapt to the misalignments d_x, d_y, and d_z in the $\mathbf{x}_1$, $\mathbf{y}_1$, and $\mathbf{z}_1$ directions, respectively. The misalignments cause the rotations of the upper arm (θ_{ap} and θ_{ay}) to be different from the output rotations of the exoskeleton (θ_p and θ_y). There is also an angle θ_{ar} to denote the internal/external (medial/lateral) rotation of the upper arm. Angles θ_{ap}, θ_{ay}, and θ_{ar} independently describe the rotation of a human upper arm.

In [2], two parallel linkages are located at the proximal end of the exoskeleton to acquire passive DOFs for shoulder alignment. The linkages must support the exoskeleton weight. Compared with [2], our passive DOFs are located at the distal end. They are achieved using a simpler and smaller mechanism that does not have to support exoskeleton weight.

2.4 Novelties and advantages of the proposed exoskeleton

Previous serial exoskeletons use rotary motors with harmonic drives [1, 3-4, 11] that are perpendicular to human body at different locations. There are moving motors that require stronger structure support and larger accommodation space. Thus the exoskeletons are big and heavy.

By contrast, the proposed linear motors are parallel to human body and placed side-by-side to minimize extruded parts. The exoskeleton output torque can be easily amplified using slider crank mechanisms and thus overly large motors or harmonic drives are avoided. The 4R and 5R spherical mechanisms make both motors grounded. They inherently have an interior hollow space to accommodate a human's shoulder. The combination of motor arrangement and spherical mechanisms makes the exoskeleton compact while maintaining sufficient rigidity, torque output, and range of motion.

We are among the first to realize both linear SEA and adaptive mechanism in upper limb exoskeletons. These two components allow adaptive and safe shoulder rehabilitation while the number of actuators and force sensors is minimized. The reduction of complexity makes our exoskeleton lightweight, which is indicated in Table 1. The exoskeleton is also less costly and easier to operate.

III. Exoskeleton Kinematics and Statics

3.1 Kinematics

Fig. 6 defines the rotation and span angles of the arc links of the 5R and 4R spherical mechanisms. For the 5R spherical mechanism, angle α_{12} is required to be 90° so that the pitch axis remains vertical with respect to the ground while the yaw mechanism can be nearly parallel to a human's back. Meanwhile, angle α_{13} is required to be 90° so that the yaw axis can be horizontal with respect to the ground. The other three angles (α_{24}, α_{35}, and α_{45}) can be independently chosen

This article has been accepted for publication in a future issue of this journal, but has not been fully edited. Content may change prior to final publication. Citation information: DOI 10.1109/TMECH.2017.2717874, IEEE/ASME Transactions on Mechatronics

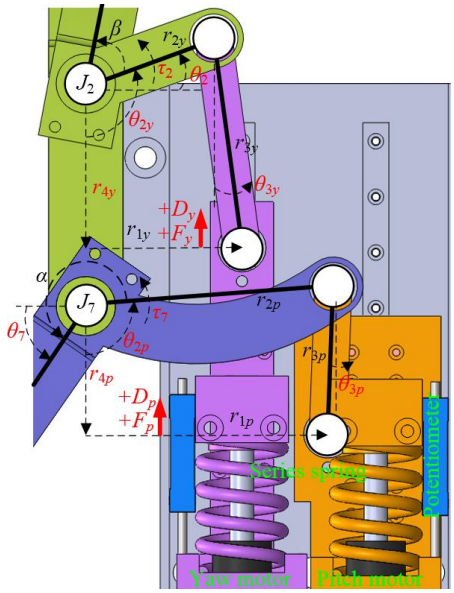

Fig. 7 Pitch and yaw mechanisms

but are ideally 90° in order to achieve maximum range of motion. However, arc links with large span angles may cause interference with human body during operation. Once the span angles are determined, a proper angle ψ is chosen to provide the desired range for the yaw motion. A nonzero ψ is required to avoid interference of Link 3 with the upper arm and adaptive mechanism. For the 4R spherical mechanism, angles α_{78} and α_{89} can also be independently chosen. Except for the fixed Link 0, the rotations of Links 1-4 are denoted as θ_1-θ_4. The rotations of Links 7 and 6 are denoted as θ_7 and θ_8, respectively. Interference of the spherical mechanisms with human body is avoided by using sufficiently large radii for the arc links.

The input rotations of θ_1 and θ_2 are provided by the pitch and yaw mechanisms shown in Fig. 7. The pitch motor displacement D_p is transmitted to rotate Link 7 with angle θ_{2p}. Similarly, the yaw motor displacement D_y is transmitted to rotate Link 2 with angle θ_{2y}. Table 2 lists the dimensions of the spherical, pitch, and yaw mechanisms used in this paper. Their values have been optimized in order to maximize the output torques τ_p and τ_y given the motor force and displacement [23].

The relationship between the motor displacements (D_p and D_y) and crank angles (θ_{2p} and θ_{2y}) can be obtained by solving the following loop closure equations.

$$r_{4p} - D_p + x_p + r_{3p}C_{3p} - r_{2p}C_{2p} = 0 \quad (1)$$

$$r_{4y} - D_y + x_y + r_{3y}C_{3y} - r_{2y}C_{2y} = 0 \quad (2)$$

In Eqs. (1-2) and rest of this paper, S and C denote the sine and cosine functions, respectively. When S and C have subscripts, they correspond to the subscripts of θ. Symbols x_p and x_y denote the deformation (positive if tension) of the springs serially connected to the pitch and yaw motors, respectively. Lengths r_{4p} and r_{4y} are defined at $\theta_p = \theta_y = 0°$. The coupler angles θ_{3p} and θ_{3y} in Eqs. (1-2) can be expressed as

$$\theta_{3p} = S^{-1}[(r_{2p}S_{2p} - r_{1p})/r_{3p}] \quad (3)$$

Table 2 Sizes of the spherical, pitch, and yaw mechanisms (units: ° or mm)

Spherical mechanisms	Pitch and yaw mechanisms
$\alpha_{12} = 90$, $\alpha_{13} = 90$	$r_{1p} = 65.05$, $r_{2p} = 66.74$, $r_{3p} =$
$\alpha_{24} = 84.82$, $\alpha_{35} = 44.93$	39.76, $r_{4p} = 34.48$, $\alpha = 230.69$,
$\alpha_{45} = 85.11$, $\psi = 23.36$	$D_p = -23.67$ to 39.33
$\alpha_{78} = 59.43$, $\alpha_{89} = 60.57$	$r_{1y} = 41.97$, $r_{2y} = 36.49$, $r_{3y} =$
	57.05, $r_{4y} = 44.27$, $\beta = 59.70$,
	$D_y = -24.57$ to 40.82

$$\theta_{3y} = S^{-1}[(r_{2y}S_{2y} - r_{1y})/r_{3y}] \quad (4)$$

The crank angles θ_{2p} and θ_{2y} are further related to angles θ_7 and θ_2 by the followings.

$$\theta_7 = \theta_{2p} + \alpha - 3\pi/2, \quad \theta_2 = \theta_{2y} + \beta - \pi/2 \quad (5)$$

Angle θ_7 is transmitted to θ_1 through the 4R spherical mechanism. The relationship between θ_7 and θ_1 can be derived using spherical trigonometry. First, the value of θ_9, the angle between Link 6 and the horizontal plane, can be obtained using the sine rule.

$$S_7 / S\alpha_{89} = S_9 / S\alpha_{78} \quad (6)$$

Then the value of θ_1 can be obtained by solving Napier's analogies.

$$T[(\alpha_{89} + \alpha_{78})/2] = \frac{C[(\theta_7 - \theta_9)/2]}{C[(\theta_7 + \theta_9)/2]} T[(\tfrac{3\pi}{2} - \theta_1)/2] \quad (7)$$

where T denotes the tangent function. Taking time derivatives of Eqs. (1-2), the angular velocities of θ_7 and θ_2 can be obtained.

$$\dot{\theta}_7 = (\dot{D}_p - \dot{x}_p)C_{3p} / r_{2p}S_{2p-3p} \quad \text{where} \quad \dot{\theta}_7 = \dot{\theta}_{2p} \quad (8)$$

$$\dot{\theta}_2 = (\dot{D}_y - \dot{x}_y)C_{3y} / r_{2y}S_{2y-3y} \quad \text{where} \quad \dot{\theta}_2 = \dot{\theta}_{2y} \quad (9)$$

Taking time derivatives of Eqs. (6-7), the angular velocity of θ_1 can be obtained as

$$\dot{\theta}_1 / \dot{\theta}_7 = S_7 / [\cot\alpha_{78} - C_7 \cot(\tfrac{3\pi}{2} - \theta_1)] \quad (10)$$

The input rotations are further transmitted to output rotations through the 5R spherical mechanism. The output rotation θ_p is related to input rotation θ_1 by

$$\theta_p = \theta_1 - 180° \quad (11)$$

and unaffected by the input angle θ_2. By observing Fig. 4, the output yaw angle can be expressed as

$$\theta_y = \theta_3 + \psi - 1.5\pi \quad (12)$$

where θ_3 is the rotation of Link 3 with respect to Link 1. The value of θ_3 can be obtained using rotation transformation matrices.

$$\theta_3 = C^{-1}\left(\frac{-z + C\alpha_{13}C\alpha_{35}}{S\alpha_{13}S\alpha_{35}}\right) \quad (13)$$

The value of z in Eq. (13) further depends on θ_1 and θ_2. Detailed expression of z can be found in [22]. Thus the output yaw angle depends on both θ_1 and θ_2. In general, the relationship between the input angular velocities and output angular velocities can be expressed as

$$\begin{bmatrix} \dot{\theta}_p \\ \dot{\theta}_y \end{bmatrix} = \begin{bmatrix} 1 & 0 \\ f_1(\theta_1,\theta_2) & f_2(\theta_1,\theta_2) \end{bmatrix} \begin{bmatrix} \dot{\theta}_1 \\ \dot{\theta}_2 \end{bmatrix} \quad (14)$$

The functions f_1 and f_2 are too lengthy and not shown.

This article has been accepted for publication in a future issue of this journal, but has not been fully edited. Content may change prior to final publication. Citation information: DOI 10.1109/TMECH.2017.2717874, IEEE/ASME Transactions on Mechatronics

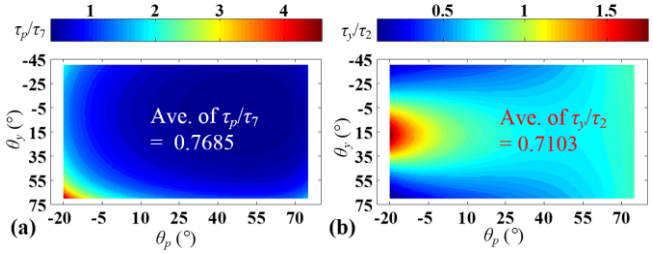

Fig. 8 (a) τ_p/τ_7 torque ratio (b) τ_y/τ_2 torque ratio

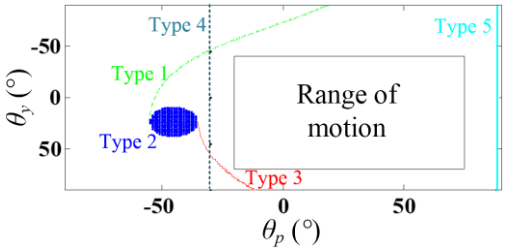

Fig. 9 Singularity analysis

3.2 Statics

In Fig. 6, the input pitch and yaw torques are denoted as τ_1 and τ_2, respectively. The input pitch torque τ_1 is further related to τ_7 of the 4R spherical mechanism by

$$\tau_1 / \tau_7 = [\cot\alpha_{78} - C_7 \cot(\tfrac{3\pi}{2} - \theta_1)] / S_7 \qquad (15)$$

The torques τ_7 and τ_1 are related to the motor forces F_p and F_y by the followings.

$$\tau_7 = r_{2p}(S_{2p-3p}/C_{3p})F_p \;;\; \tau_2 = r_{2y}(S_{2y-3y}/C_{3y})F_y \qquad (16)$$

where θ_{2p}, θ_{2y}, θ_{3p}, and θ_{3y} can be obtained using Eqs. (1-4). The output pitch and yaw torques are further related to the input torques by

$$\begin{bmatrix} \tau_p \\ \tau_y \end{bmatrix} = \begin{bmatrix} 1/C_y & f_3(\theta_1,\theta_2) \\ 0 & f_4(\theta_1,\theta_2) \end{bmatrix} \begin{bmatrix} \tau_1 \\ \tau_2 \end{bmatrix} \qquad (17)$$

According to Eq. (17), the output pitch torque is contributed by both the input pitch and yaw torques, whereas the output yaw torque solely depends on the input yaw torque. This arrangement is good because therapeutic exercises mostly require the yaw motion (flexion/extension and abduction/adduction). The output yaw torque is unaffected by the input pitch torque, which makes control of the yaw torque easier. Since the yaw torque needs to support any unbalanced gravity force, the load requirement on the yaw motor is larger than that of the pitch motor.

To evaluate the mechanical advantage of the spherical mechanisms, Figs. 8(a) and 8(b) show the diagrams of the torque ratios of the pitch and yaw directions, respectively. The average torque ratios of both directions are comparable. The variation of τ_p/τ_7 within the range of motion is much smaller while the variation of τ_y/τ_2 is greater. In the yaw direction, the torque ratio is much smaller near the positive and negative extremes of θ_y. To further increase the average of torque ratio τ_y/τ_2, the span angle α_{35} should be increased.

3.3 Singularity analysis

Based on the kinematics and statics presented in Secs. 3.1-3.2, the singular positions of the 5R and 4R spherical mechanisms can be analyzed. For the 5R spherical mechanism, the singular positions refer to the cases where the

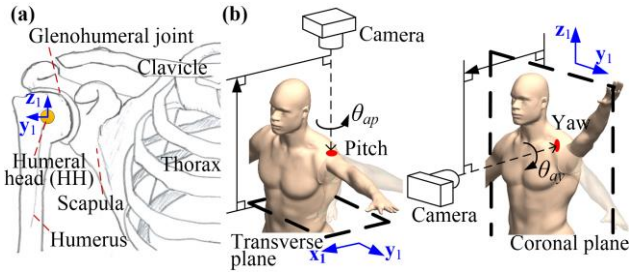

Fig. 10 (a) Skeleton diagram of human shoulder (b) Experiment setup to measure the HH displacements

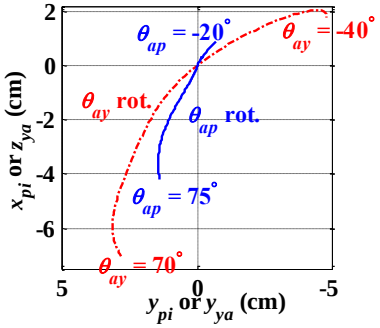

Fig. 11 Displacements of the HH during the θ_{ap} and θ_{ay} rotations (S_2)

2×2 matrix in Eq. (14) or (17) has a determinant equal to zero ($f_2 = 0$ or $f_4 = 0$). There are three types of singularities that would affect normal operation of the exoskeleton. Using the parameters in Table 2, Fig. 9 shows the θ_p-θ_y curves of the three types of singularities. The desired range of motion, namely $\theta_p = -20°$ to 75° and $\theta_y = -40°$ to 70°, is indicated as a rectangular box. Types 1 and 3 singularities denote cases where Links 3 and 4 are coplanar ($\theta_5 = 180°$ for Type 1 and 0° for Type 3). The torque ratio τ_y/τ_2 in the yaw direction would be zero ($f_4 = 0$). Type 1 occurs when θ_y is smaller than −57° whereas Type 3 occurs when θ_p is less than −24°. Type 2 singularity denotes the case where Links 2 and 4 are coplanar with $\theta_4 = 180°$. The torque ratio τ_y/τ_2 would be infinity ($f_2 = 0$). This case occurs when θ_p is less than −35°. Since the exoskeleton may be driven by the motors (forward) or upper arm (inverse), all these singular positions need to be avoided. Among the three types, Type 3 curve is the closest to the range of motion. The link sizes of the 5R spherical mechanism have been chosen such that the singularity curves are moved to the left of the range of motion. Comparing Figs. 8(b) and 9, moving thee three singularity curves toward the left can also minimize the variation of the torque ratio τ_y/τ_2 near the negative extreme of θ_p.

In Fig. 9, Types 4 and 5 are the two singular positions of the 4R spherical mechanism. They can be obtained by setting the denominator in Eq. (15) equal to zero. Type 4 occurs at $\theta_p = -30°$, which corresponds to $\theta_7 = 0°$ and $\theta_8 = 180°$ with torque ratio τ_1/τ_7 in the pitch direction equal to infinity. Type 5 occurs at $\theta_p = 89°$, which corresponds to $\theta_7 = 180°$ and $\theta_8 = 0°$ with torque ratio τ_1/τ_7 also equal to infinity. These singularities need to be avoided when the exoskeleton is driven by the upper arm. Compared with Types 1-3, Types 4-5 of the 4R spherical mechanism are unrelated to the yaw motion and are away from the range of pitch motion.

This article has been accepted for publication in a future issue of this journal, but has not been fully edited. Content may change prior to final publication. Citation information: DOI 10.1109/TMECH.2017.2717874, IEEE/ASME Transactions on Mechatronics

Table 3 Misalignment range of the HH

	S_1	S_2	S_3
Range of d_x (mm)	−54 to 25	−60 to 58	−55 to 38
Range of d_y (mm)	−33 to 74	−38 to 54	−32 to 44
Range of d_z (mm)	−48 to 22	−42 to 26	−70 to 21

IV. Design of Shoulder Adaptive Mechanism

4.1 Humeral head (HH) displacements

As Fig. 10(a) shows, the center of the glenohumeral (GH) joint is denoted as the humeral head (HH). In Fig. 5, the GH joint was modeled as a spherical joint and HH was denoted as O_h. We assumed in Sec. 2 that the HH coincides with the center O_1 of the 5R spherical mechanism and has negligible displacements when the humerus moves. In practice, the displacements of the HH increase with the increase of motion range of the upper arm. The humerus is connected to the thorax through the scapula and clavicle. Assuming that the thorax is stationary, the scapula and clavicle would have three-dimensional translation and rotation motions when the upper arm rotates, which would make the HH to displace in the $\mathbf{x}_1$, $\mathbf{y}_1$, and $\mathbf{z}_1$ directions. Non-negligible HH displacements would cause significant misalignment problems.

4.2 Measurement of humeral head displacements

To study the effect of upper arm rotation on the HH displacements, an experiment with setup shown in Fig. 10(b) was conducted. The experiment was to measure the displacements of the HH during θ_{ap} and θ_{ay} rotations. A red marker was attached closest to the surface of the HH and a camera was aligned with the $\mathbf{x}_1\mathbf{y}_1\mathbf{z}_1$ frame to measure the displacements of the marker with respect to the rotation of the upper arm. Three different healthy subjects were tested. The subject heights were 1700, 1750, and 1850 mm for S_1 to S_3, respectively. For the θ_{ap} rotation, the upper arm rotated from $\theta_{ap} = -20°$ to 75° while $\theta_{ay} = 0°$. The displacements of HH were denoted as x_{pi} and y_{pi}. For the θ_{ay} rotation, the upper arm rotated from $\theta_{ay} = -40°$ to 70° while $\theta_{ap} = 90°$. The displacements of HH were denoted as y_{ya} and z_{ya}. It was noted in [24] that the HH displacements during the θ_{ay} rotation was almost independent of θ_{ap}. Thus we used the result of $\theta_{ap} = 90°$ to represent the HH displacements during the θ_{ay} rotation for all values of θ_{ap}.

Fig. 11 shows the average of repeated measurements of S_2. The HH has more significant x_{pi} than y_{pi} displacements for the θ_{ap} rotation along the $\mathbf{z}_1$ axis. For the θ_{ay} rotation along the $\mathbf{x}_1$ axis, the HH has more significant z_{ya} than y_{ya} displacements. The overall displacement of θ_{ay} rotation is greater than θ_{ap} rotation. When the upper arm has a combined rotation of θ_{ap} and θ_{ay}, the HH would displace three-dimensionally. The misalignments d_x, d_y, and d_z are related to the measured displacements by the followings.

$$d_x = y_{ya}\cos\theta_{ap} + x_{pi}$$
$$d_y = y_{ya}\sin\theta_{ap} + y_{pi};\ d_z = z_{ya} \quad (18)$$

Using Eq. (18), we obtained the misalignment ranges of the three subjects for $\theta_{ap} = -20°$ to 75° and $\theta_{ay} = -40°$ to 70°. The ranges are listed in Table 3. The misalignment ranges are not small and should be taken into account when designing the adaptive mechanism.

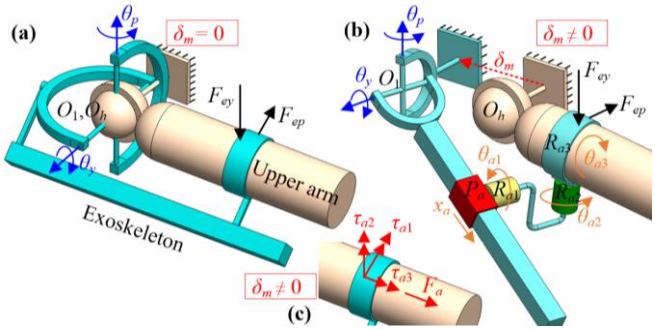

Fig. 12 Schematic of exoskeleton-arm connection: (a) without misalignment (b) adding passive joints with misalignment (c) undesirable forces and moments when misaligned

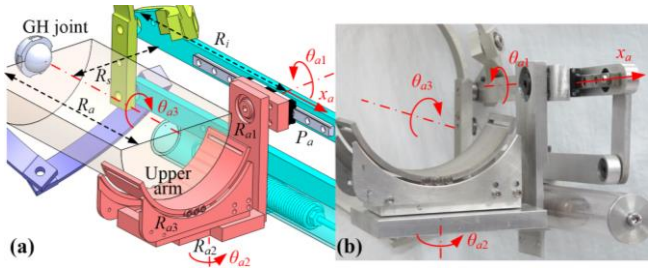

Fig. 13 (a) CAD model of the adaptive mechanism (b) Prototype

4.3 Mobility analysis and design of the adaptive mechanism

Fig. 12(a) shows the schematic of exoskeleton-limb connection. Our exoskeleton with two active DOFs can be modeled as a link connected at a universal joint. Using the definition in Fig. 2(b), the center of the universal joint is denoted as O_1. A human humerus can be ideally considered as a rigid rod connected at a spherical joint with center at O_h. When mounting the exoskeleton on a human's shoulder, the exoskeleton is rigidly attached to the upper arm and it is required that the rotation centers of the exoskeleton (O_1) and humerus (O_h) coincide. Thus the combination can be treated as a paradoxical over-constrained system [25] with two active DOFs. The actuation of the pitch and yaw motors in the exoskeleton can drive the upper arm to generate the pitch and yaw motions. As shown in Fig. 12(a), the driving forces in the pitch and yaw directions are F_{ep} and F_{ey}, respectively.

In practice, O_1 and O_h may not coincide due to the HH displacements mentioned in Sec. 4.2. Fig. 12(b) shows a configuration where the two centers are not aligned. The separation δ_m depends on the orientation of the upper arm and hence varies. When δ_m is not zero, the mobility becomes −1. The exoskeleton and arm together become a statically indeterminate (hyperstatic) structure that cannot move. Because there will be tissue deformation in the shoulder, the upper arm can still be driven by the exoskeleton. However, the exoskeleton would cause harmful constraint force/moment to human upper arm. Fig. 12(c) shows the possible constraint force (F_a) and moments (τ_{a1}, τ_{a2}, and τ_{a3}) that are undesirable. The magnitude of the harmful constraint force/moment increases with the increase of separation between O_1 and O_h.

This article has been accepted for publication in a future issue of this journal, but has not been fully edited. Content may change prior to final publication. Citation information: DOI 10.1109/TMECH.2017.2717874, IEEE/ASME Transactions on Mechatronics

To adapt to the HH displacements, the whole system must recover its mobility of two. Thus three extra DOFs are required. As shown in Fig. 12(b), the connection between the exoskeleton and upper arm is designed with three serially connected passive joints. Translation joint P_a allows the relative sliding motion of the upper arm along the exoskeleton. Rotation joints R_{a1} and R_{a2} allow the relative rotation between the exoskeleton and the upper arm. The displacements are denoted as x_a, θ_{a1}, and θ_{a2}, respectively. These three passive joints can remove the constraint force F_a and moments τ_{a1}/τ_{a2} shown in Fig. 12(c).

To further remove the constraint moment τ_{a3}, another rotation joint R_{a3} is required. As shown in Fig. 12(b), the rotation of R_{a3} is denoted as θ_{a3}. This joint allows free internal/external rotation of the upper arm with respect to the exoskeleton. Totally there are four passive joints at the interface. Ref. [15] also proposed similar concept of passive joints.

Fig. 13(a) shows the CAD model of the adaptive mechanism that offers the four passive joints. In order to minimize the constraint force/moment, the adaptive mechanism is placed closest to the interface between the exoskeleton and upper arm. Symbol R_i denotes the distance from O_1 to P_a joint at the neutral position while R_a denotes the distance from the GH joint to the position where the upper arm is attached to the adaptive mechanism. When O_h and O_1 are aligned, R_i is equal to R_a. Fig. 13(b) shows a prototype of the adaptive mechanism.

4.4 Kinematics of the adaptive mechanism

Given the rotation angles (θ_p, θ_y) of the exoskeleton and the misalignments (d_x, d_y, and d_z) of the shoulder center, the upper arm rotation angles (θ_{ap}, θ_{ay}) can be obtained using homogenous transformation matrices.

$$\theta_{ap} = T^{-1}\left(\frac{S_p C_{a2} C_{y-a1} + S_{a2} C_p}{C_p C_{a2} C_{y-a1} - S_{a2} S_p}\right) \tag{19}$$

$$\theta_{ay} = S^{-1}(S_{y-a1} C_{a2}) \tag{20}$$

The angles θ_{a1} and θ_{a2} of the passive joints in Eqs. (19-20) can be expressed as

$$\theta_{a1} = -S^{-1}[(d_z C_y + d_x C_p S_y + d_y S_p S_y)/(R_a C_{a2})] \tag{21}$$

$$\theta_{a2} = S^{-1}[(d_x S_p - d_y C_p)/R_a] \tag{22}$$

Once θ_{a1} and θ_{a2} are determined, the displacement x_a can be obtained as

$$x_a = R_a C_{a1} C_{a2} - (R_i + d_z S_y - d_x C_p C_y - d_y C_y S_p) \tag{23}$$

Angle θ_{a3} is a function of the arm roll angle θ_{ar}

$$\theta_{a3} = T^{-1}\left(\frac{-S_{ar} C_{ap-p} + S_{ay} C_{ar} S_{ap-p}}{C_{ar} C_{ap-p} + S_{ay} S_{ar} S_{ap-p}}\right) \tag{24}$$

where the arm roll angle θ_{ar} can be inversely expressed as

$$\theta_{ar} = T^{-1}\left(\frac{-S_{a3} C_{a1-y} + S_{a2} C_{a3} S_{y-a1}}{C_{a3} C_{a1-y} + S_{a2} S_{a3} S_{y-a1}}\right) \tag{25}$$

The angle θ_{a3} is used to adapt to the independent rotation of θ_{ar}. When aligned, it can be shown that $\theta_{a3} = -\theta_{ar}$.

It can be observed in Eq. (22) that θ_{a2} is independent of θ_y and d_z. In Eqs. (21-22) and (24), θ_{a1}, θ_{a2}, and θ_{a3} are all independent of x_a. When there is no misalignment ($d_x = d_y = d_z = 0$), it can be concluded from Eqs. (21-23) that $\theta_{a1} = \theta_{a2} = x_a = 0$. Inversely, Eqs. (19-22) can be used to numerically solve for θ_p, θ_y, θ_{a1}, and θ_{a2} given θ_{ap}, θ_{ay}, d_x, d_y, and d_z. The value of x_a can then be obtained using Eq. (23).

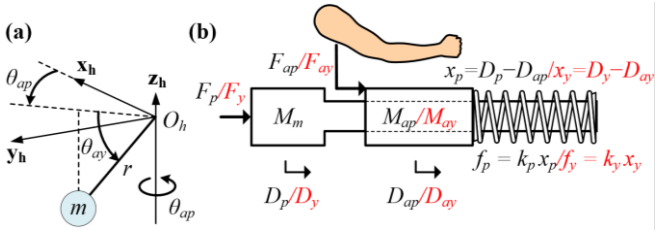

Fig. 14 (a) Upper arm model (b) Model of the pitch and yaw motion with SEA

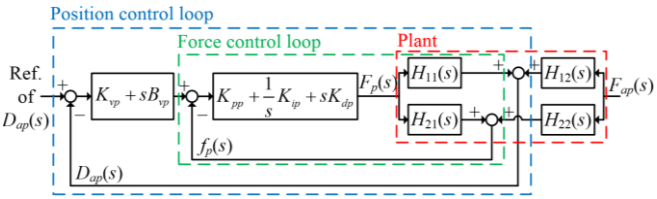

Fig. 15 Impedance control diagram of the pitch motion

Based on the measurements in Sec. 4.2, we can obtain the ranges of x_a, θ_{a1}, and θ_{a2}. Within the range of exoskeleton motion, the ranges are $x_a = -27.8$ to 80.5 mm, $\theta_{a1} = -19.2°$ to 5.0°, and $\theta_{a2} = -21.8°$ to 8.6°. The design of the adaptive mechanism needs to ensure sufficient displacements of the three passive joints without causing interference. If exact rotation of the upper arm is required, sensors can be added to measure the displacements of the passive joints. The displacements are used to compute d_x, d_y, and d_z using Eqs. (21-23). In addition, θ_{ap} and θ_{ay} are computed using Eqs. (19-20).

Taking time derivatives of Eqs. (19-20), the relationship between the arm angular velocities and exoskeleton angular velocities can be expressed as

$$[\dot{\theta}_{ap} \quad \dot{\theta}_{ay}]^T = \mathbf{J}[\dot{\theta}_p \quad \dot{\theta}_y]^T \tag{26}$$

where the components of $\mathbf{J}$ are functions of R_a, d_x, d_y, d_z, θ_{a1}, θ_{a2}, θ_p, and θ_y. Using the principle of virtual work, the actual torques (τ_{ap}, τ_{ay}) applied on the upper arm are related to the output pitch and yaw torques by

$$\begin{bmatrix} \tau_{ap} \\ \tau_{ay} \end{bmatrix} = \mathbf{J}^{-T} \begin{bmatrix} C_y & -C_y f_3 / f_4 \\ 0 & 1 \end{bmatrix} \begin{bmatrix} \tau_p \\ \tau_y \end{bmatrix} \tag{27}$$

Observing Figs. 12(a-b), τ_{ap} and τ_{ay} are further related to the driving forces F_{ep} and F_{ey} by

$$\tau_{ap} = R_a F_{ep}\ ;\ \tau_{ay} = R_a F_{ey} \tag{28}$$

For our current adaptive mechanism, we have $R_a = R_i = 180$ mm and $R_s = 105$ mm.

4.5 Merits of the adaptive mechanism

By using the adaptive mechanism, precise alignment between the exoskeleton and upper arm is no longer necessary. This can reduce the setup time. The displacement of shoulder center and variation among different subjects can be allowed using the four passive joints. Compared with those using active joints [3, 4] to account for the displacement of shoulder center, the use of the proposed adaptive mechanism does not require additional actuators and hence the

This article has been accepted for publication in a future issue of this journal, but has not been fully edited. Content may change prior to final publication. Citation information: DOI 10.1109/TMECH.2017.2717874, IEEE/ASME Transactions on Mechatronics

Table 4 Impedance controller gains

Pitch	K_{vp} = 50 N/mm; B_{vp} = 1 Ns/mm; K_{pp} = 0.65, K_{ip} = 10 s^{-1}, K_{dp} = 0.05 s
Yaw	K_{vy} = 50 N/mm; B_{vy} = 1 Ns/mm; K_{py} = 2.9, K_{iy} = 12 s^{-1}, K_{dy} = 0.04 s

complexity can be greatly reduced. The adaptive mechanism is quicker and more stable when reacting to any involuntary shoulder shrugging of patients in rehabilitation exercises.

V. Dynamic Model, Control, and Experiments

5.1 Dynamic model

Fig. 14(a) shows the model of the upper arm. We consider an unaligned upper arm with mass m and distance r from O_h to the center of mass. Fig. 14(b) shows the model of the exoskeleton and SEA in the pitch and yaw directions. The symbol M_m is the reflected rotor mass of the motor. We define M_{ap} and M_{ay} as the reflected masses of the upper arm as seen by the pitch and yaw motors, respectively.

$$M_{ap} = I_{ap}h_{p1}^2 + I_{ay}h_{p2}^2 \; ; \; M_{ay} = I_{ap}h_{y1}^2 + I_{ay}h_{y2}^2 \tag{29}$$

where

$$I_{ap} = \tfrac{1}{2}m(r\cos\theta_{ay})^2 \; ; \; I_{ay} = \tfrac{1}{2}mr^2 \; ; \; h_{p1} = \partial\theta_{ap}/\partial D_{ap}$$
$$h_{p2} = \partial\theta_{ay}/\partial D_{ap} \; ; \; h_{y1} = \partial\theta_{ap}/\partial D_{ay} \; ; \; h_{y2} = \partial\theta_{ay}/\partial D_{ay} \tag{30}$$

The coupling of the pitch and yaw directions appear in the h_{p2} and h_{y1} terms. The displacements of M_{ap} and M_{ay} are denoted as D_{ap} and D_{ay}, respectively. They are related to the motor displacements D_p and D_y by

$$x_p = D_p - D_{ap} \; ; \; x_y = D_y - D_{ay} \tag{31}$$

The masses of other components are small and hence can be ignored. By doing so, both the pitch and yaw motions can be modeled as a two-inertia system: M_m and M_{ap} for the pitch motion while M_m and M_{ay} for the yaw motion.

Considering an aligned case where r = 135 mm and m = 2.44 kg, the reflected mass of the upper arm can be calculated using Eq. (29). In the pitch direction, the average value of M_{ap} is 37.5 kg in the range of motion. In the yaw direction, the average value of M_{ay} is 95.5 kg. Both M_{ap} and M_{ay} are larger than the reflected rotor mass (M_m = 18.19 kg). The average value of M_{ay} is larger because the mechanical advantage in the yaw direction is largely smaller.

There are two inputs in each direction: one from the motor (F_p or F_y) and the other from the upper arm (F_{ap} or F_{ay}). Both inputs are defined along the motor axis. Neglecting friction and damping, the dynamic equations in the pitch and yaw directions can be respectively derived as follows.

$$F_p - k_p x_p = M_m \ddot{D}_p \; ; \; F_{ap} + k_p x_p = M_{ap}\ddot{D}_{ap} \tag{32}$$

$$F_y - k_y x_y = M_m \ddot{D}_y \; ; \; F_{ay} + k_y x_y = M_{ay}\ddot{D}_{ay} \tag{33}$$

In Eqs. (32-33), the terms $k_p x_p$ and $k_y x_y$ denote the spring forces f_p and f_y, respectively. They can be obtained given the values of x_p and x_y measured using the potentiometers. The values of D_{ap} and D_{ay} are calculated using Eq. (31), where D_p and D_y are measured using the encoders.

5.2 Impedance controller

The pitch motion in Eq. (32) can be rewritten in a state-space form as

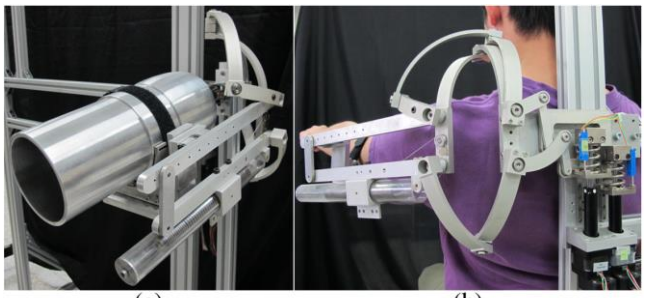

(a) (b)

Fig. 16 (a) The exoskeleton with a dummy arm (b) Prototype of the exoskeleton on a human limb

$$\mathbf{Y}(s)/\mathbf{U}(s) = \mathbf{H}(s) = [H_{11}(s)\; H_{12}(s); H_{21}(s)\; H_{22}(s)] \tag{34}$$

where $\mathbf{Y} = [D_{ap}(s)\; f_p(s)]^T$, $\mathbf{U} = [F_p(s)\; F_{ap}(s)]^T$, and

$$H_{11} = k_p/[M_m M_{ap} s^4 + k_p(M_m + M_{ap})s^2]$$
$$H_{21} = M_{ap}k_p/[M_m M_{ap} s^2 + k_p(M_m + M_{ap})]$$
$$H_{12} = H_{11}(M_m s^2 + k_p)/k_p \; ; \; H_{22} = -H_{21}M_m/M_{ap}$$

Our linear SEAs can be used for different types of compliance controllers that require accurate force control. As an illustration, we consider a cascaded impedance controller in the pitch direction. As the diagram in Fig. 15 shows, the impedance controller includes an inner force controller and an outer position controller. The PD gains K_{vp} and B_{vp} are the coefficients of the virtual spring and damper connected between an upper arm and exoskeleton. By changing the values K_{vp} and B_{vp}, different interface impedance can be provided during the rehabilitation process. The state-space equations governing the yaw motion and the corresponding impedance control law can be derived in the same fashion.

Given a set of K_{vp} and B_{vp}, the PID gains K_{pp}, K_{ip}, and K_{dp} in the inner loop are tuned to achieve stability within the range of motion while the performance is not sacrificed. Table 4 lists the parameters of the controller gains. Subscripts p and y are used to denote gains in the pitch and yaw directions, respectively. A value of K_{vp} = 50 N/mm represents a virtual spring stiffness of 50 N/mm between the exoskeleton and upper arm. The value of K_{vp} should be small enough to provide interface compliance. However, smaller K_{vp} would reduce the accuracy and bandwidth of position control.

In Fig. 15, the force F_p from the pitch motor assists the force F_{ap} from the upper arm to trace a reference trajectory of D_{ap}. The amount of F_{ap} depends on the ability of a patient's upper arm. The larger the value of F_{ap} is, the smaller the required pitch motor force is to mobilize the upper arm. Hence the proposed impedance controller can be used for patients with different levels of ability to mobilize their arms. The value of F_{ap} can be obtained using Eq. (32) to evaluate arm force recovery.

5.3 Prototype

Fig. 16(a) shows a prototype of the exoskeleton with a dummy arm (made of Aluminum alloy). This dummy is connected to the exoskeleton center through a spherical joint. Similar to a normal human upper arm, the dummy has a length of 286.8 mm and weight of 1.86 kg. It will be used for testing of the exoskeleton. Fig. 16(b) shows the exoskeleton attached to the left arm of an ordinary person with height of

This article has been accepted for publication in a future issue of this journal, but has not been fully edited. Content may change prior to final publication. Citation information: DOI 10.1109/TMECH.2017.2717874, IEEE/ASME Transactions on Mechatronics

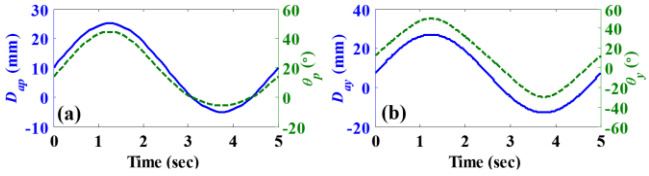

Fig. 17 Reference trajectories
(a) D_{ap} and θ_p (b) D_{ay} and θ_y

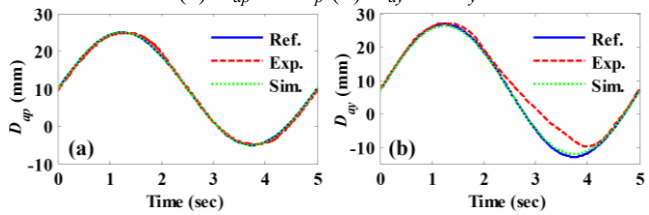

Fig. 18 Experimental results of position control
(a) Pitch at $\theta_y = 0°$ (b) Yaw at $\theta_p = 0°$

1750 mm. For rehabilitation purposes, the exoskeleton is placed on a stationary base so that the person does not have to support the weight of the exoskeleton. By using the adaptive mechanism proposed in Sec. 4, the alignment between the exoskeleton and human shoulder does not have to be very accurate. Since the arm weight is nearly balanced, the yaw motor only needs to provide a minimum force to overcome the friction forces at the joints and any unbalanced weight.

5.4 Impedance control experiment

Based on the setup in Fig. 16(a), experiments have been conducted to verify the impedance controller performance. Using the parameters listed in Table 4, the experiments were implemented in NI cRIO 9066 with a sampling frequency of 1 kHz. We first performed rotation control experiment where the exoskeleton rotated the dummy arm to trace a reference sinusoidal trajectory in either the pitch or yaw direction. This experiment was used to emulate the scenario where the exoskeleton mobilizes a patient's upper limb during the initial stage of rehabilitation (passive mode, based on the patient's activity). Figs. 17(a) and 17(b) show the 0.2-Hz reference trajectories of D_{ap} and D_{ay}, respectively. The corresponding trajectories of θ_p and θ_y are also shown. They were computed using the equations in Sec. 3.1. Figs. 18(a) and 18(b) show the simulation and experimental results in the pitch and yaw directions, respectively. The experimental curves have traced the reference ones well. In Fig. 18(b), the slight mismatch of the experimental yaw curve with the simulation and reference curves was due to motor saturation. If the reference frequency was below 0.2 Hz, then the experimental yaw curve would match with the reference curve well. Using a motor of larger power can overcome the problem of saturation to increase the response speed in the yaw direction. The pitch motion has a larger mechanical advantage and hence the pitch controller can trace a reference frequency up to 0.4 Hz without having motor saturation.

The same experiments can be repeated for different values of K_{vp} and K_{vy}. Smaller values of K_{vp} and K_{vy} are preferable if the interaction safety needs to be ensured. However, smaller values of K_{vp} and K_{vy} make the exoskeleton appear softer when viewed from the human side and hence would cause larger position control tracking error.

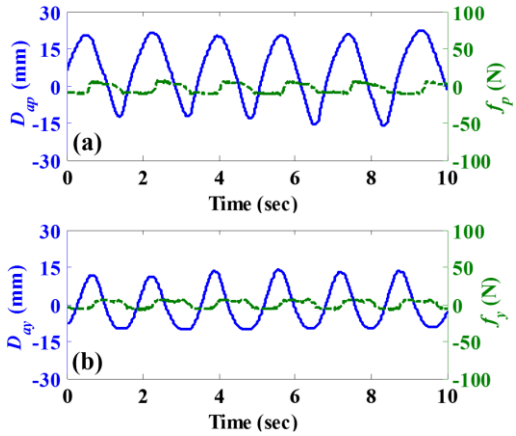

Fig. 19 Experiment results of zero impedance control
(a) Pitch at $\theta_y = 0°$ (b) Yaw at $\theta_p = 0°$

Table 5 Passive joint displacements due to misalignment (units in mm or °)

Position	Calculated	Measured	Error
$\theta_p = 0.0$ $\theta_y = 2.5$	$x_a = 32.6$	$x_a = 29$	11.2%
	$\theta_{a1} = -17.5$	$\theta_{a1} = -18$	2.8%
	$\theta_{a2} = 16.1$	$\theta_{a2} = 12$	25.6%
$\theta_p = 9.5$ $\theta_y = -7.9$	$x_a = 32.4$	$x_a = 29$	10.5%
	$\theta_{a1} = -14.9$	$\theta_{a1} = -15$	0.7%
	$\theta_{a2} = 18.7$	$\theta_{a2} = 15$	19.6%
$\theta_p = 19.8$ $\theta_y = 17.9$	$x_a = -8.4$	$x_a = -3$	64.3%
	$\theta_{a1} = -19.7$	$\theta_{a1} = -20$	1.3%
	$\theta_{a2} = 20.8$	$\theta_{a2} = 17$	18.4%

To further stimulate limb recovery, a patient must be able to move his upper limb with partial or no assistance from the exoskeleton (assistive or active mode). To share the limb action, the exoskeleton must be back-drivable. To demonstrate the back-drivability of our exoskeleton, we make both K_{vp} and B_{vp} equal to zero. In this case, there should be zero impedance between the upper limb and exoskeleton. The upper limb should be able to move freely. Using the same experiment setup as that in Fig. 16(a), the dummy arm was manually given a sinusoid-like motion with frequency of 0.6 Hz and amplitude of 15 mm. Figs. 19(a) and 19(b) show the results of zero impedance control in the pitch and yaw directions, respectively. Because zero impedance was used, the SEAs should be controlled to have zero spring force regardless of the dummy arm motion. The f_p and f_y values in Figs. 19(a-b) are very small. The residual spring force with root mean square value less than 7 N was mainly due to the friction force in the motors. Because the exoskeleton is back-drivable, using zero impedance control allows the recording of a limb's autonomous movement with minimal influence.

5.5 Kinematic misalignment experiment

Using the setup in Fig. 16(a), we presented a kinematic misalignment test. The test was to verify the displacements of the passive joints due to a given misalignment where $d_x = 50$, $d_y = -50$, and $d_z = 50$ mm. The displacements of the passive joints were measured using angle/linear rulers. Table 5 lists the values of x_a, θ_{a1}, and θ_{a2} at three distinct positions. The

This article has been accepted for publication in a future issue of this journal, but has not been fully edited. Content may change prior to final publication. Citation information: DOI 10.1109/TMECH.2017.2717874, IEEE/ASME Transactions on Mechatronics

three positions were selected based on small to large angle magnitudes. The calculated displacements of the passive joints were obtained using Eqs. (21-23). The measured displacements generally agreed with the calculated ones, which verified our kinematic model in Sec. 4.4. The displacement errors were primarily due to the accumulated clearance of the joints (linear and rotary bearings). Hence larger passive joint displacements tended to have smaller errors than smaller passive joint displacements.

5.6 Misalignment force experiment

As can be observed in Fig. 11, the HH displacement is larger in the yaw direction. To study the effect of the adaptive mechanism on the force between the upper limb and exoskeleton, we have conducted yaw rotation control experiments (passive mode) using the same three subjects as those in Sec. 4.2. The experiment setup and reference trajectory of 0.1 Hz are shown in Figs. 20(a) and 20(b), respectively. We used the same impedance controller and parameters as those in Sec. 5.2. The shoulder center O_h of each subject was placed as close as possible to the exoskeleton center O_1. Hence the misalignment was primarily due to the HH displacements of each subject. The subjects were instructed not to exert physical force during the experiment. Values of the yaw spring force f_y with locked passive joints were measured and compared against those with unlocked passive joints. We define the increase of f_y as

$$\begin{aligned}\text{Increase of } f_y = {} & f_y \text{ of locked passive joints} \\ & - f_y \text{ of unlocked passive joints}\end{aligned} \tag{35}$$

The average and maximum increases of f_y are shown in Fig. 21. If an unaligned dummy arm was used for the experiment, the increase of f_y would reach infinity because the exoskeleton and upper limb form a statically indeterminate structure. Unlike the dummy arm, human upper limbs are relatively deformable. Hence the increase of f_y would be limited. Still, Fig. 21 shows a significant increase of f_y among different subjects. The average increase of f_y is nearly 20 N and the maximum increase can reach up to 60 N. Accordingly, the constraint force/moment between the locked passive joints and upper arm would significantly increase as well, which results in uncomfortable and even harmful interaction.

To use the exoskeleton in practice, a therapist can hold a subject's arm to complete a comfortable trajectory of θ_{ap} and θ_{ay} using zero impedance. A computer simultaneously records the corresponding θ_p and θ_y. The exoskeleton can then be programmed to repeatedly follow the recorded trajectory of θ_p and θ_y using adjustable impedance. The corresponding limb rotations θ_{ap} and θ_{ay} can then be precisely controlled to follow what the therapist did.

VI. Conclusions

This paper has presented a parallel actuated exoskeleton for after-stroke shoulder rehabilitation. Due to the arrangement of the parallel, slider-crank, and gravity-balancing mechanisms, this 2-DOF shoulder exoskeleton can be made small-size and lightweight while the range of motion and output torque are still comparable to previous shoulder exoskeletons [1, 2, 8, 9]. The exoskeleton with the proposed adaptive mechanism has been demonstrated to accommodate

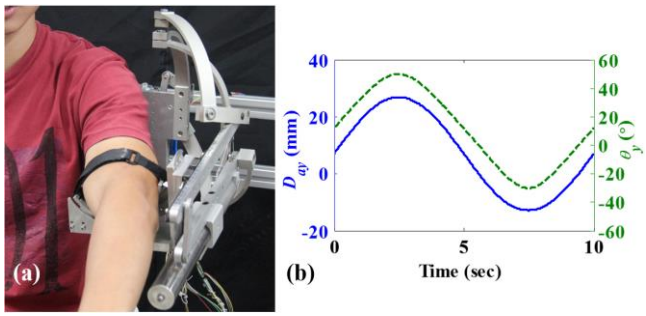

Fig. 20 (a) Experimental setup to measure the spring force due to misalignment (b) Reference trajectory of 0.1 Hz

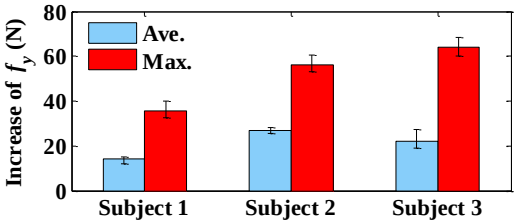

Fig. 21 Increase of f_y due to HH displacements with locked passive joints

subjects with height variation from 1700 to 1850 mm. Misalignments between the shoulder and exoskeleton can be allowed while unsafe constraint forces can be minimized using only passive joints. The passive and active mode experiments have demonstrated the ability of the exoskeleton to provide motion control while maintaining at a prescribed impedance. Based on the proposed design, actuation of the shoulder internal/external rotation and elbow flexion/extension can be serially added to achieve full control of an upper limb. Our future work includes clinical tests and evaluations. We expect that the proposed exoskeleton can provide rehabilitation for people with disabled shoulder functions.

References

[1] T. Nef, M. Guidali, and R. Riener, 2009, "ARMin III–arm therapy exoskeleton with an ergonomic shoulder actuation," Applied Bionics and Biomechanics, 6(2), 127-142.

[2] A. Otten et al., 2015, "LIMPACT: a hydraulically powered self-aligning upper limb exoskeleton," IEEE/ASME transactions on mechatronics, 20(5), 2285-2298.

[3] S.-H. Chen et al., 2016, "Assistive control system for upper limb rehabilitation robot," IEEE Transactions on Neural Systems and Rehabilitation Engineering.

[4] B. Kim and D. D. Ashish, 2015, "Controls for the shoulder mechanism of an upper-body exoskeleton for promoting scapulohumeral rhythm," IEEE ICORR, 538-542.

[5] K. Xu, J. Zhao, D. Qiu, and Y. Wang, 2014, "A pilot study of a continuum shoulder exoskeleton for anatomy adaptive assistances," Journal of Mechanisms and Robotics, 6(4), 041011.

[6] N. Vitiello et al., 2016, "Functional design of a powered elbow orthosis towards its clinical employment," IEEE/ASME Transactions on Mechatronics, 21(4), 1880-1891.

[7] A. U. Pehlivan, F. Sergi, and M. K. O'Malley, 2015, "A subject-adaptive controller for wrist robotic rehabilitation," IEEE/ASME Transactions on Mechatronics, 20(3), 1338-1350.

[8] H. Kim et al., 2012, "Redundancy resolution of the human arm and an upper limb exoskeleton," IEEE Transactions on Biomedical Engineering, 59(6), 1770-1779.

[9] J. Klein et al., 2010, "Optimization of a parallel shoulder mechanism to achieve a high-force, low-mass, robotic-arm exoskeleton," IEEE

Transactions on Robotics, 26(4), 710-715.
[10] Y. Jung and J. Bae, 2015, "Kinematic analysis of a 5-dof upper-limb exoskeleton with a tilted and vertically translating shoulder joint," IEEE/ASME Transactions on Mechatronics, 20(3), 1428-1439.
[11] U. Keller et al., 2016, "ChARMin: The first actuated exoskeleton robot for pediatric arm rehabilitation." IEEE/ASME Transactions on Mechatronics.
[12] Y. Mao and S. K. Agrawal, 2012, "Design of a cable-driven arm exoskeleton (CAREX) for neural rehabilitation," IEEE Transactions on Robotics, 28(4), 922-931.
[13] P.-C. Kung et al., 2016, "Control of forearm module in upper-limb rehabilitation robot for reduction and biomechanical assessment of pronator hypertonia of stroke patients," Journal of Mechanics in Medicine and Biology, 16(02), 1650008.
[14] S. J. Housman et al., 2007, "Arm-training with T-WREX after chronic stroke: preliminary results of a randomized controlled trial," IEEE ICORR, 562-568.
[15] N. Jarrassé and G. Morel, 2012, "Connecting a human limb to an exoskeleton," IEEE Transactions on Robotics, 28(3), 697-709.
[16] M. Cempini et al., 2013, "Self-alignment mechanisms for assistive wearable robots: A kinetostatic compatibility method," IEEE Transactions on Robotics, 29(1), 236-250.
[17] P. Maciejasz et al., 2014, "A survey on robotic devices for upper limb rehabilitation," Journal of Neuroengineering and Rehabilitation, 11(1), 1.
[18] J. Huang et al., 2015, "Control of upper-limb power-assist exoskeleton using a human-robot interface based on motion intention recognition," IEEE Transactions on Automation Science and Engineering, 12(4), 1257-1270.
[19] Y.-F. Lee et al., 2016, "A Humanoid robotic wrist with two-dimensional series elastic actuation for accurate force/torque interaction," IEEE/ASME Transactions on Mechatronics, 21(3), 1315-1325.
[20] H. Vallery et al., 2008, "Compliant actuation of rehabilitation robots," IEEE Robotics & Automation Magazine, 15(3).
[21] A. H. Stienen et al., 2010, "Design of a rotational hydroelastic actuator for a powered exoskeleton for upper limb rehabilitation," IEEE Transactions on biomedical engineering, 57(3), 728-735.
[22] H.-C. Hsieh, L. Chien, and C.-C. Lan, 2015, "Mechanical design of a gravity-balancing wearable exoskeleton for the motion enhancement of human upper limb," IEEE ICRA, 4992-4997.
[23] H.-C. Hsieh, L. Chien, and C.-C. Lan, 2015, "Dimensional synthesis of a lightweight shoulder exoskeleton," IEEE AIM, 670-675.
[24] P. M. Ludewig et al., 2009, "Motion of the shoulder complex during multiplanar humeral elevation," Journal of Bone & Joint Surgery 91(2), 378-389.
[25] G. Gogu, 2005, "Mobility of mechanisms: a critical review," Mechanism and Machine Theory, 40(9), 1068-1097.

Hsiang-Chien Hsieh received his B.S. and M.S. degrees in mechanical engineering from National Cheng Kung University, Taiwan, in 2013 and 2015, respectively. His previous research interests were exoskeleton design, robotics, and machine learning.

Dian-Fu Chen received his B.S. degree in mechanical engineering from National Chiao Tung University, Taiwan, in 2014 and M.S. degree in mechanical engineering from National Cheng Kung University, Taiwan, in 2016. His previous research interests were mechanism design, robotics, and automation.

Li Chien received his B.S. and M.S. degrees in mechanical engineering from National Cheng Kung University, Taiwan, in 2014 and 2016, respectively. His previous research interests were control systems, mechatronics, and robotics.

Chao-Chieh Lan (M'09, SM'15) received his B.S. degree in mechanical engineering from National Taiwan University, Taiwan, in 2000 and Ph.D. degree in mechanical engineering from Georgia Institute of Technology in 2006. He is currently a professor in the Department of Mechanical Engineering at National Cheng Kung University, Taiwan. He is currently interested in compliant actuators, robotics, multi-body dynamics, and rehabilitation devices.